Alloying Nickel with Molybdenum Significantly Accelerates Alkaline Hydrogen Electrocatalysis

Miao Wang[+], Hao Yang[+], Jinan Shi, Yufeng Chen, Yuan Zhou, Liguang Wang, Sijia Di, Xuan Zhao, Jun Zhong, Tao Cheng, Wu Zhou, and Yanguang Li*

Abstract: Bifunctional hydrogen electrocatalysis (hydrogen-oxidation and hydrogen-evolution reactions) in alkaline solution is desirable but challenging. Among all available electrocatalysts, Ni-based materials are the only non-precious-metal-based candidates for alkaline hydrogen oxidation, but they generally suffer from low activity. Here, we demonstrate that properly alloying Ni with Mo could significantly promote its electrocatalytic performance. Ni_4Mo alloy nanoparticles are prepared from the reduction of molybdate-intercalated Ni-$(OH)_2$ nanosheets. The final product exhibits an apparent hydrogen-oxidation activity exceeding that of the Pt benchmark and a record-high mass-specific kinetic current of $79\,A\,g^{-1}$ at an overpotential of 50 mV. A superior hydrogen-evolution performance is also measured in alkaline solution. These experimental data are rationalized by our theoretical simulations, which show that alloying Ni with Mo significantly weakens its hydrogen adsorption, improves the hydroxyl adsorption and decreases the reaction barrier for water formation.

Hydrogen is generally regarded as an ideal energy carrier for connecting the intermittent renewable energy with the diverse consumer market.[1,2] Its electrochemical conversion is realized via two fundamental and important reactions, namely hydrogen evolution reaction (HER) and hydrogen oxidation reaction (HOR).[3] The former transforms electric energy to chemical energy, and takes place at the cathode of water electrolyzers, whereas the latter releases energy stored in

[*] M. Wang,[+] Dr. H. Yang,[+] Y. Chen, Y. Zhou, S. Di, X. Zhao, Prof. J. Zhong, Prof. T. Cheng, Prof. Y. Li
Institute of Functional Nano & Soft Materials (FUNSOM), Jiangsu Key Laboratory for Carbon-Based Functional Materials and Devices, Soochow University
Suzhou 215123 (China)
E-mail: yanguang@suda.edu.cn

Dr. J. Shi, Prof. W. Zhou
School of Physical Sciences University of Chinese Academy of Sciences
Beijing 100049 (China)

Dr. L. Wang
Key Laboratory of Carbon Materials of Zhejiang Province, Institute of New Materials and Industrial Technologies, Wenzhou University
Wenzhou, Zhejiang 325035 (China),
and
Department of Chemistry and Biochemistry, University of Windsor
Windsor, ON N9B3P4 (Canada)

[+] These authors contributed equally to this work.

Supporting information and the ORCID identification number(s) for the author(s) of this article can be found under:
https://doi.org/10.1002/anie.202013047.

chemical bonds and finds its important application in fuel cells. Despite the prohibitive cost, Pt (and also its alloys) represents the best candidate for both HER and HOR electrocatalysis owing to its optimal surface binding with the reaction intermediate (*H, where * denotes surface adsorption) as dictated by the Sabatier principle.[4] It is so far the catalyst of choice for commercially available proton exchange membrane (PEM) fuel cells and PEM electrolyzers. Over recent years, an increasing interest is placed on alkaline fuel cells and alkaline electrolyzers for their lower costs and higher energy conversion efficiency.[5,6] This prompts the active search for efficient alkaline hydrogen electrocatalysts.[7–10] Unfortunately, the HER/HOR rate on Pt is typically orders of magnitude slower in bases than in acids,[11] which essentially compromises its performance advantage over other materials. There is thereby a large incentive to develop non-precious-metal-based (NPM) alternatives with comparable activities in alkaline solution and at a fractional cost of the precious metal benchmark.

Compared to the large variety of NPM electrocatalysts for alkaline HER reported in literature, Ni-based materials are so far the only available NPM candidates for alkaline HOR in our best knowledge.[12–14] Pristine Ni has little HOR and HER activities, which are mainly constrained by its relatively strong surface affinity toward *H as revealed by computational simulations.[15,16] In addition, pristine Ni is far from ideal to promote water formation and dissociation that is often proposed to be the rate-determining step (although different views exist) for alkaline HOR and HER.[14] Many strategies have been accordingly developed to modulate the electronic structure of Ni, and tune its interaction with reaction intermediates via, for example, alloying with other metals or nonmetals,[16–18] modifying with metal oxides[19,20] or coupling with conductive supports.[21,22] Our group recently demonstrated that the interstitial nitrogen doping in Ni_3N weakened the *H binding, and enabled active and durable HOR in alkaline solution with excellent mass activity and CO tolerance.[16] Hu and co-workers reported that the H_2 pyrolysis of Ni-containing metal-organic frameworks gave rise to strained Ni nanoparticles, which under the optimal condition exhibited state-of-the-art mass activity of $50\,A\,g^{-1}$ for alkaline HOR at the overpotential (η) of 50 mV.[23] Despite all these progresses, there is still much room for improvement in order to narrow the performance gap between Ni and Pt.

In this contribution, we report that alloying Ni with Mo represents a viable strategy to significantly accelerate bifunctional HOR and HER in alkaline solution. Ni-Mo alloys have been investigated as an alkaline HER electrocatalyst with the

earliest works dating back to the 1980s by Brown and co-workers.[24,25] Their potential for HOR, however, is rarely explored and remains elusive.[26] Here, we prepare Ni$_4$Mo alloy nanoparticles from the reduction of molybdate-intercalated Ni(OH)$_2$ nanosheets. The final product demonstrates apparent HOR activity exceeding the Pt benchmark and record-high mass-specific kinetic current of 79 A g^{-1} at $\eta =$ 50 mV as well as excellent HER activity.

Ni$_4$Mo alloy nanoparticles were prepared by a two-step precipitation-reduction approach (Figure 1a). For the first step, stoichiometric Ni(NO$_3$)$_2$ and (NH$_4$)$_6$Mo$_7$O$_{24}$ were reacted and co-precipitated by ammonia in ethylene glycol. X-ray diffraction (XRD) analysis of the product from this step (denoted as NiMoOH) reveals a diffraction pattern resembling α-Ni(OH)$_2$ (Supporting Information Figure S1a).[27] Its in-plane (100) and (110) diffraction peaks remain at the same position as α- or β-Ni(OH)$_2$, whereas its (00l) peaks shift toward the low angle direction with the (001) peak locating at $2\theta = 7.8°$, corresponding to a large interlayer distance of 1.1 nm. This value is considerably larger than that of regular α-Ni(OH)$_2$ with nitrate or carbonate intercalates ($d \approx 0.8$ nm)[28] or β-Ni(OH)$_2$ with no intercalate ($d \approx 0.46$ nm),[28] evidencing the intercalation of a bulky anion presumably MoO$_4^{2-}$. The molybdate intercalation is also supported from the signature vibration modes of MoO$_4^{2-}$ between 300 cm^{-1} and 1000 cm^{-1} in the Raman spectrum (Figure S1b).[29,30] Scanning electron microscopy (SEM) characterization shows that NiMoOH consists of hierarchical nanosheet assemblies. Individual nanosheets are about micrometer-wide and < 10 nm thick, and are often curved or wrinkled (Figure S1c,d).

In the second step, NiMoOH was annealed in 10% H$_2$/Ar at 400°C for its complete reduction to form the desirable bimetallic alloy. XRD pattern of the final product displays broad diffraction peaks similar to cubic-phase Ni but reproducibly displaced by 0.6–1.2° to the low angle side (Figure 1b). It is best assignable to body-centered tetragonal Ni$_4$Mo (ICDD 03-065-5480). From the prominent (121) peak, the particle size is estimated to be ≈9 nm based on the Sherrer's formula. SEM imaging unveils that NiMoOH nanosheets from the first step are transformed to interconnected nanoparticles upon reduction with the overall hierarchical structure largely preserved (Figure 1c). The particle size is measured to be 5–10 nm from TEM (Figure 1d), in good agreement with the above XRD analysis. Furthermore, aberration-corrected scanning transmission electron microscopy (STEM) of Ni$_4$Mo alloy nanoparticles was performed. From the high-angle annular dark-field (HAADF) imaging as shown in Figures 1e,f, we are able to clearly resolve the atomic arrangements that are consistent with the standard Ni$_4$Mo model in the (120) and (−13−5) view. Lattice fringes of 0.21 nm and 0.18 nm as labelled correspond to the (121) and (310) interplanar distance of Ni$_4$Mo, respectively. These alloy nanoparticles are analyzed to contain abundant grain boundaries. Unfortunately, we are unable to further distinguish Ni and Mo atoms based on their HAADF intensity due to the superposition of Ni and Mo atoms in the out-of-plane direction and the irregular particle shape. Elemental mapping under energy dispersive X-ray spectroscopy (EDS) indicates the high spatial correlation between Ni and Mo species, and thereby suggests the formation of a uniform alloy instead of undesirable phase segregation (Figure 1g–i). BET measurement reveals that Ni$_4$Mo nanoparticles have surface areas of 52.8 m^2 g^{-1} (Supporting Information Figure S2). Inductively coupled plasma (ICP) analysis concludes that the Ni/Mo atomic ratio in the final product is 4.06.

Different experimental parameters were explored for their influences on the final products. Pure Ni nanoparticles were prepared as the control without adding the Mo precursor under otherwise identical conditions. Structural characterization shows that they are extensively aggregated with substantially larger particle size (30–100 nm) (Supporting Information Figure S3) and smaller surface areas (20.5 m^2 g^{-1}) (Figure S2). Varying the nominal Ni/ Mo ratio from 20 to 2 gives rise to the similar morphology and XRD pattern as Ni$_4$Mo (Supporting Information Figure S4). In addition, we find that 300°C is the lowest temperature for the complete reduction of NiMoOH to Ni$_4$Mo, while raising the temperature to 500°C leads to the emergence of a new phase
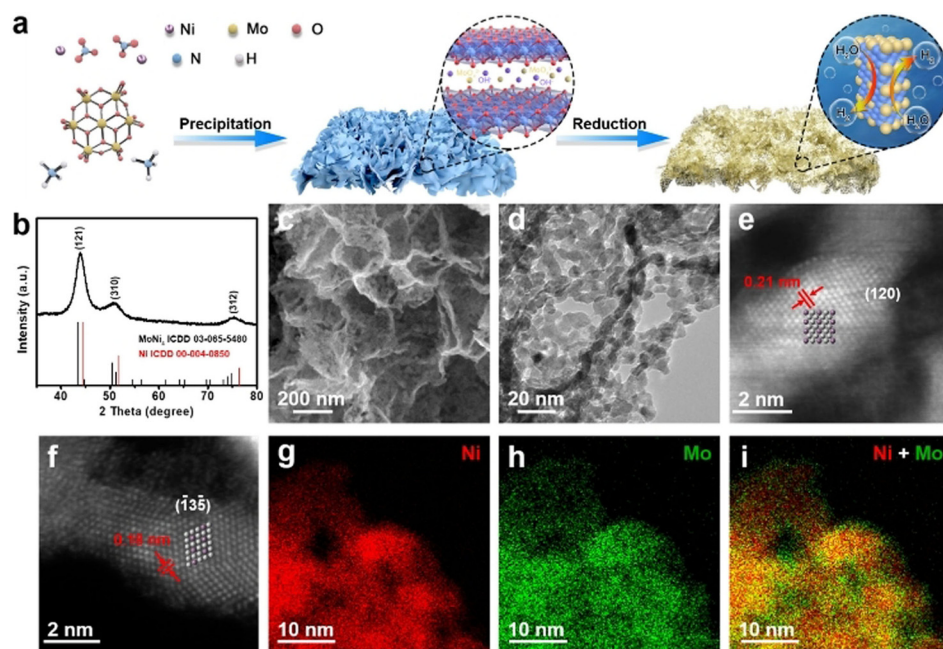

Figure 1. Preparation and structural characterizations of Ni$_4$Mo nanoparticles. a) Schematic synthetic procedure of Ni$_4$Mo nanoparticles; b) XRD pattern, c) SEM image, d) TEM image and e,f) STEM-HAADF images of Ni$_4$Mo; g–i) EDS elemental mapping of Ni and Mo in Ni$_4$Mo.

5772   www.angewandte.org

© 2020 Wiley-VCH GmbH

Angew. Chem. Int. Ed. **2021**, *60*, 5771–5777

assignable to NiMo (ICDD 00-048-1745) (Figure S4).

To probe the local chemical environment and bonding configuration of Ni_4Mo, we carried out X-ray photoelectron spectroscopy (XPS) and X-ray absorption spectroscopy (XAS) studies of the alloy nanoparticles. The Mo 3d XPS spectrum of Ni_4Mo contains a broad envelope of peaks, which can be deconvoluted to four sets of doublets from Mo^0, Mo^{4+}, Mo^{5+} and Mo^{6+} with their $3d_{5/2}$ peaks centered at 228.0 eV, 229.1 eV, 230.5 eV and 232.2 eV, respectively (Figure 2 a).[31,32] The pronounced signals of high-valent Mo species are contributed from the superficial oxide film formed upon air exposure. The Ni 2p XPS spectra of Ni_4Mo and Ni exhibit a similar feature with the Ni $2p_{3/2}$ peak positioned at 852.5 eV assignable to metallic Ni (Figure 2 b). The Mo K edge X-ray absorption near-edge structure (XANES) of Ni_4Mo is shown to have an adsorption edge close to that of the Mo foil reference but slightly displaced toward the higher energy side due to its surface oxide (Figure 2 c). The corresponding Fourier transform extended X-ray absorption fine structure (EXAFS) reveals mainly the Mo-Ni bonding contribution (Supporting Information Table S1), in good agreement with previous publications[33] and distinctive from the Mo-Mo bonding observed for the metallic Mo reference (Figure 2 d). Moreover, the Ni K edge XANES spectra of Ni_4Mo and Ni show absorption edges similar to that of the Ni foil reference (Figure 2 e). However, the chemical environment around Ni atoms is analyzed to be slightly different in Ni_4Mo compared to metallic Ni as reflected from their corresponding EXAFS spectra (Figure 2 f). Fitting the data with the Ni_4Mo model gives rise to an average Ni-Ni coordination number of 7.7 and an average Ni-Mo coordination number of 2.9 in alloy nanoparticles (Table S1).

Next, we evaluated the electrocatalytic HOR performance of Ni_4Mo in H_2-saturated 0.1 M KOH. For standard measurements, its catalyst loading on the glassy carbon rotating disk electrode (RDE) was controlled at 0.2 $mg_{(metal)} cm^{-2}$. Commercial 20 wt% Pt/C and 20 wt% PtRu/C at the loading of 10 $\mu g_{(metal)} cm^{-2}$ were introduced as the precious metal benchmarks for comparison side by side. It should be noted that PtRu/C represents the best alkaline HOR electrocatalyst available so far with an activity two to three times higher than Pt/C through a bifunctional mechanism.[34] When rotated at 1600 rpm, the polarization curve of PtRu/C quickly rises to the saturation current density (J) of 2.6 $mA cm^{-2}$ at $\eta = 50$ mV (Figure 3 a). The anodic current density of Pt/C increases more mildly and delivers 1.8 $mA cm^{-2}$ at $\eta = 50$ mV. These two results are in line with earlier observations.[16] Pristine Ni nanoparticles exhibit poor HOR activity with $J = 0.2 mA cm^{-2}$ at $\eta = 50$ mV. By contrast, our Ni_4Mo alloy nanoparticles demonstrate remarkable apparent HOR activity and reach the current density of 2.2 $mA cm^{-2}$ at $\eta = 50$ mV, even larger than Pt/C. and approaching PtRu/C. In our best knowledge, this represents the greatest apparent HOR activity ever reported for any NPM electrocatalysts[16,19,21,23,35] and evidences the great potential of Ni_4Mo to replace Pt for practical applications. Its HOR
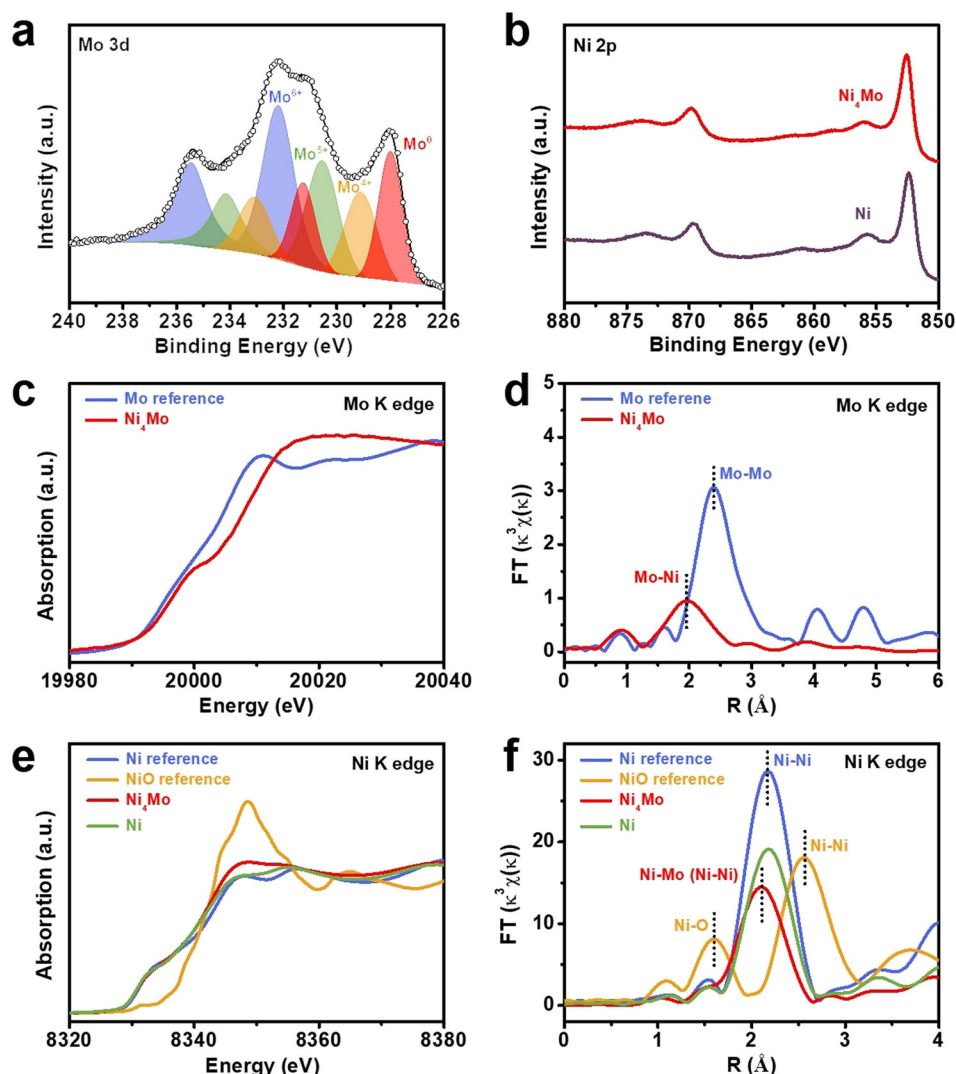

Figure 2. Spectroscopic characterizations of Ni_4Mo nanoparticles. a) High-resolution Mo 3d XPS spectrum of Ni_4Mo with proper peak deconvolution; b) high-resolution Ni 2p XPS spectrum of Ni_4Mo in comparison with Ni; c) Mo K-edge XANES spectrum and d) corresponding EXAFS spectrum of Ni_4Mo in comparison with the Mo reference; e) Ni K-edge XANES spectra and f) EXAFS spectra of Ni_4Mo and Ni in comparison with the Ni and NiO references.
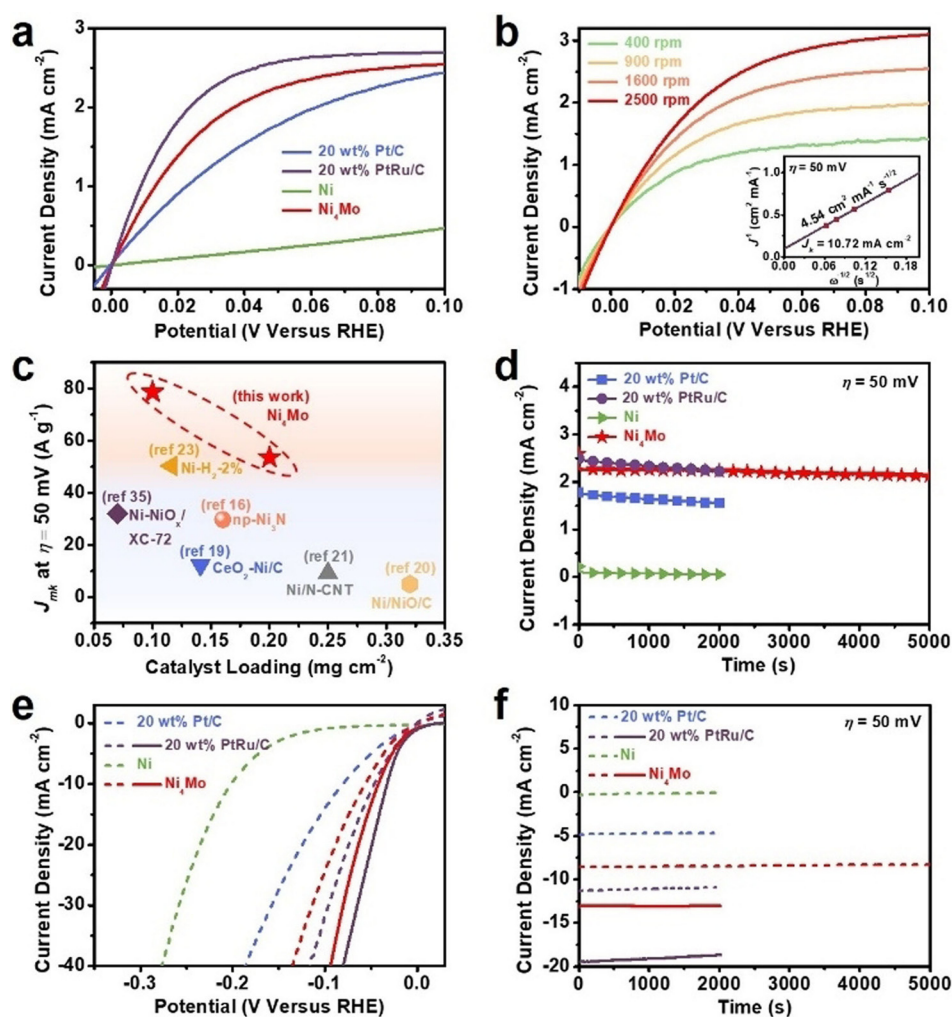
Figure 3. Hydrogen electrocatalysis of Ni_4Mo in alkaline solution. a) HOR polarization curves of Ni_4Mo, Ni, 20 wt% Pt/C and 20 wt% PtRu/C at 1600 rpm in H_2-saturated 0.1 M KOH; b) HOR polarization curves of Ni_4Mo at different electrode rotation speeds, inset shows the corresponding Koutecky-Levich plot at $\eta = 50$ mV; c) comparison of the mass-specific kinetic current of Ni_4Mo at $\eta = 50$ mV with those of previous reports; d) chronoamperometric responses of Ni_4Mo, Ni, 20 wt% Pt/C and 20 wt% PtRu/C at 1600 rpm and $\eta = 50$ mV; e) HER polarization curves of Ni_4Mo, Ni, 20 wt% Pt/C and 20 wt% PtRu/C in (dotted) 0.1 M KOH and (solid) 1 M KOH; f) chronoamperometric responses of Ni_4Mo, Ni, 20 wt% Pt/C and 20 wt% PtRu/C in (dotted) 0.1 M KOH and (solid) 1 M KOH at -50 mV versus RHE.

as described by the Koutecky-Levich equation. Its extrapolation to $\omega^{-1/2} = 0$ gives rise to a kinetic current density (J_k) of 10.72 mA cm^{-2} and a mass-specific kinetic current (J_{mk}) of 53.6 A g^{-1} (Figure 3b inset). Both values are even larger than the previous state of the art reported by Hu and co-workers (Figure 3b and Supporting Information Table S2).[23] Importantly, we want to emphasize that owing to the lack of reliable methods to determine the electrochemical active surface (ECSA) of Ni, we are not comfortable here to normalize the current density over ECSA like what previous works did for comparison. In addition, the exchange current density (J_0) of Ni_4Mo nanoparticles is derived to be 2.82 mA cm^{-2} by fitting the Butler-Volmer equation in the micropolarization region (Supporting Information Figure S8). Corresponding mass-specific exchange current (J_{m0}) is calculated to be 14.1 A g^{-1}, about half of the previous states of the art.[23,35] Note that both J_{mk} and J_{m0} values are dependent on the catalyst loading. To this end, we also prepared Ni_4Mo electrodes at 0.1 mg cm^{-2} (similar to Hu's work) for HOR (Supporting Information Figure S9). Lowering the catalyst loading sacrifices the apparent activity with $J = 2.0$ mA cm^{-2} recorded at $\eta = 50$ mV, whereas their J_{mk} and J_{m0}

activity starts to decline when anodically polarized over 0.2 V (versus reversible hydrogen electrode or RHE, the same hereinafter) owing to the Ni oxidation (Figure S5). Further increasing the catalyst loading to 0.4 mg$_{(metal)}$ cm^{-2} promotes the current density to 2.44 mA cm^{-2} at $\eta = 50$ mV (Figure S6). Control experiments show that when the Mo content is too little (Ni/Mo = 20) or too much (Ni/Mo = 2) or when the annealing temperature is lower (300°C) or higher (500°C), the measured HOR activities of alloy products are all significantly worse (Supporting Information Figure S7).

As a step further, the mass activity of Ni_4Mo nanoparticles was derived. Figure 3b shows the HOR polarization curves under different electrode rotation rates. By plotting and fitting the inverse of the current density (J^{-1}) at $\eta = 50$ mV versus the inverse of the square root rotation rate ($\omega^{-1/2}$), a straight line is obtained with the slope of 4.54 cm^2 mA^{-1} s$^{-1/2}$

are promoted to 78.7 A g^{-1} and 26.1 A g^{-1}, respectively—both are clearly superior to all previous works (Figure 3c and Table S2). We believe that these two values can be pushed to the possible limit by further decreasing the catalyst loading. However, this would require the time-consuming optimization of the catalyst ink formulation and is not pursued here.

The stability of Ni_4Mo nanoparticles was assessed by biasing the working electrode at $\eta = 50$ mV while continuously rotating it at 1600 rpm. As shown in Figure 3d, our electrocatalyst delivers a stable current density of 2.2 mA cm^{-2} throughout the test. This is contrasted by the gradual activity loss of both Pt/C and PtRu/C. After 2000 s, the anodic current density of PtRu/C is even surpassed by that of Ni_4Mo nanoparticles.

After concluding about the excellent HOR performance of Ni_4Mo nanoparticles, we continued to examine their

potential for HER in alkaline solution, which is the reverse reaction of HOR. The development of bifunctional HER and HOR electrocatalysts are essential to unitized regenerative fuel cells, which can operate under either the electrolyzer mode or the fuel cell mode for reversible hydrogen generation and utilization.[36] We first ran the experiments in 0.1 M KOH, and observed a similar activity trend as HOR. The cathodic current density of Ni_4Mo (0.2 $mg_{(metal)}$ cm^{-2}) takes off at about 0 V, quickly rises with the increasing overpotential and reaches 10 $mA\,cm^{-2}$ at -56 mV (Figure 3e). Its potential at $J = 10$ $mA\,cm^{-2}$ is markedly more positive than that of Ni nanoparticles (-202 mV), even better than that of Pt/C (-81 mV) and closely approaching that of PtRu/C (-47 mV). Moreover, we switched the electrolyte to 1 M KOH—a more common electrolyte for alkaline HER. The increasing solution alkalinity further improves the HER activity: it now only requires -42 mV for Ni_4Mo to reach $J = 10$ $mA\,cm^{-2}$, slightly inferior to PtRu/C (-33 mV). The HER activity of our Ni_4Mo nanoparticles exceeds all other NPM electrocatalysts under similar conditions as far as we are aware (Table S3).[37–42] Great HER stability on RDE is also observed for Ni_4Mo nanoparticles when biased at -50 mV in 0.1 M KOH or 1 M KOH (Figure 3f). Higher HOR/HER activities and longer stability are attainable by using carbon fiber paper as the current collector (Figure S10). XRD and SEM characterizations of Ni_4Mo nanoparticles after the stability tests indicate no obvious compositional or morphological change (Figure S11).

In order to gain more insights into the origin of the great electrocatalytic performance, density functional theory (DFT) calculations were performed to simulate the elementary steps of HER/HOR on Ni_4Mo. The hydrogen binding free energy (ΔG_{H*}) was first calculated. It is determined to be -0.30 eV on Ni(111) in good agreement with earlier results (Figure 4a).[43] By contrast, ΔG_{H*} on Ni_4Mo(211) (the most stable plane) is predicted to be -0.09 eV, much closer to the ideal value ($\Delta G_{H*} = 0$) for both HOR and HER. This evidences that alloying Ni with Mo can significantly weaken its hydrogen adsorption energy. *H adsorption still takes place on the Ni site but becomes destabilized due to the presence of the neighboring Mo atom (Figure 4b).

Above simulations do not actually consider the pH effect. Even though the fundamental mechanism for HOR in alkaline solution is still under heated debate, strong experimental and computational evidence suggests that the presence of surface *OH is of great significance to enhance alkaline HOR electrocatalysis.[44–47] Hence we here also calculated the adsorption energy of *OH (ΔG_{OH*}) on Ni_4Mo and pure Ni for comparison. As shown in Figure 4c, ΔG_{OH*} is predicted to be -1.01 eV on Ni_4Mo, which is remarkably more stable than that of pristine Ni (-0.09 eV). The optimized adsorption configuration shows that surface *OH binds to the highly oxophilic Mo site adjacent to Ni (Figure 4d). Based on this result, we propose that the *OH coverage on Ni_4Mo is increased and would greatly benefit alkaline HOR. At last, growing experimental results also suggest that the reaction between surface adsorbed *OH and *H to form H_2O is the rate-determining step of alkaline HOR.[44,48] To this end, we investigated the reaction kinetics
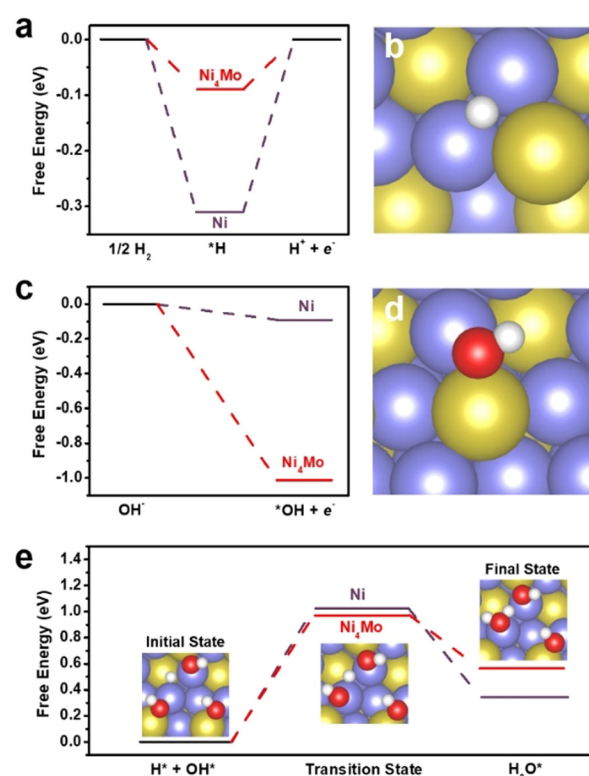

Figure 4. DFT simulations of the HER and HOR processes on Ni_4Mo-(211) and Ni(111). a) Gibbs free energy profiles for hydrogen adsorption (ΔG_{H*}) on Ni_4Mo and Ni; b) optimized hydrogen adsorption configuration on Ni_4Mo; c) Gibbs free energy profiles for hydroxyl adsorption (ΔG_{OH*}) on Ni_4Mo and Ni; d) optimized hydroxyl adsorption configuration on Ni_4Mo; e) energy barrier for water formation on Ni_4Mo and Ni, the inset illustrates the initial, final and key transition states on Ni_4Mo. Purple, yellow, red and white balls correspond to Ni, Mo, O and H atoms, respectively.

by exploring the reaction barrier of water formation from CI-NEB calculations. The barrier height is calculated to be 1.03 eV on Ni and is decreased to 0.95 eV after the introduction of Mo in Ni_4Mo (Figure 4e). Above calculations strongly support our experimental observations. It should also be noted that other opinion does exist about the promoting effect of Mo during hydrogen electrocatalysis.[49]

In summary, we reported the preparation of Ni_4Mo alloy nanoparticles via a two-step precipitation-reduction approach. The final product consisted of interconnected nanoparticles of 5–10 nm. Their intermetallic nature was characterized by multiple microscopic and spectroscopic techniques. Electrochemical measurements revealed that these alloy nanoparticles had remarkable apparent HOR activity with $J = 2.2$ $mA\,cm^{-2}$ at $\eta = 50$ mV, which was even larger than that of Pt/C and approaching that of PtRu/C. The mass-specific kinetic current and mass-specific exchange current were calculated to be $J_{mk} = 78.7$ $A\,g^{-1}$ and $J_{m0} = 26.1$ $A\,g^{-1}$ at $\eta = 50$ mV, superior to all previously reported NPM electrocatalysts in our best knowledge. Moreover, Ni_4Mo nanoparticles also exhibited great activity ($J = 10$ $mA\,cm^{-2}$ at -42 mV in 1 M KOH) and stability for alkaline HER. DFT calculations suggested that alloying Ni

with Mo significantly weakened its *H adsorption, improved the *OH adsorption and decreased the reaction barrier for water formation. Our study here highlights the great potential and practical viability of Ni-based alloys for bifunctional hydrogen electrocatalysis in alkaline solution.

Conflict of interest

The authors declare no conflict of interest.

[1] J. A. Turner, *Science* **2004**, *305*, 972–974.
[2] S. Chu, A. Majumdar, *Nature* **2012**, *488*, 294–303.
[3] V. R. Stamenkovic, D. Strmcnik, P. P. Lopes, N. M. Markovic, *Nat. Mater.* **2017**, *16*, 57–69.
[4] Z. W. Seh, J. Kibsgaard, C. F. Dickens, I. B. Chorkendorff, J. K. Norskov, T. F. Jaramillo, *Science* **2017**, *355*, eaad4998.
[5] H. A. Firouzjaie, W. E. Mustain, *ACS Catal.* **2020**, *10*, 225–234.
[6] C. Hu, L. Zhang, J. Gong, *Energy Environ. Sci.* **2019**, *12*, 2620–2645.
[7] X. Tian, P. Zhao, W. Sheng, *Adv. Mater.* **2019**, *31*, 1808066.
[8] N. Mahmood, Y. Yao, J. W. Zhang, L. Pan, X. Zhang, J. J. Zou, *Adv. Sci.* **2018**, *5*, 1700464.
[9] Y. Zheng, Y. Jiao, A. Vasileff, S. Z. Qiao, *Angew. Chem. Int. Ed.* **2018**, *57*, 7568–7579; *Angew. Chem.* **2018**, *130*, 7690–7702.
[10] M. Zeng, Y. Li, *J. Mater. Chem. A* **2015**, *3*, 14942–14962.
[11] J. Zheng, W. C. Sheng, Z. B. Zhuang, B. J. Xu, Y. S. Yan, *Sci. Adv.* **2016**, *2*, e1501602.
[12] E. S. Davydova, S. Mukerjee, F. Jaouen, D. R. Dekel, *ACS Catal.* **2018**, *8*, 6665–6690.
[13] Y. Cong, B. Yi, Y. Song, *Nano Energy* **2018**, *44*, 288–303.
[14] A. G. Oshchepkov, G. Braesch, A. Bonnefont, E. R. Savinova, M. Chatenet, *ACS Catal.* **2020**, *10*, 7043–7068.
[15] W. Sheng, M. Myint, J. G. Chen, Y. Yan, *Energy Environ. Sci.* **2013**, *6*, 1509–1512.
[16] T. Wang, M. Wang, H. Yang, M. Xu, C. Zuo, K. Feng, M. Xie, J. Deng, J. Zhong, W. Zhou, T. Cheng, Y. Li, *Energy Environ. Sci.* **2019**, *12*, 3522–3529.
[17] A. Roy, M. R. Talarposhti, S. J. Normile, I. V. Zenyuk, V. De Andrade, K. Artyushkova, A. Serov, P. Atanassov, *Sustainable Energy Fuels* **2018**, *2*, 2268–2275.
[18] W. Sheng, A. P. Bivens, M. Myint, Z. Zhuang, R. V. Forest, Q. Fang, J. G. Chen, Y. Yan, *Energy Environ. Sci.* **2014**, *7*, 1719–1724.
[19] F. Yang, X. Bao, P. Li, X. Wang, G. Cheng, S. Chen, W. Luo, *Angew. Chem. Int. Ed.* **2019**, *58*, 14179–14183; *Angew. Chem.* **2019**, *131*, 14317–14321.
[20] Y. Yang, X. Sun, G. Han, X. Liu, X. Zhang, Y. Sun, M. Zhang, Z. Cao, Y. Sun, *Angew. Chem. Int. Ed.* **2019**, *58*, 10644–10649; *Angew. Chem.* **2019**, *131*, 10754–10759.
[21] Z. Zhuang, S. A. Giles, J. Zheng, G. R. Jenness, S. Caratzoulas, D. G. Vlachos, Y. Yan, *Nat. Commun.* **2016**, *7*, 10141.
[22] P. A. Simonov, O. V. Cherstiouk, A. N. Kuznetsov, V. I. Zaikovskii, T. Y. Kardash, A. G. Oshchepkov, A. Bonnefont, E. R. Savinova, *J. Electroanal. Chem.* **2019**, *852*, 113551.
[23] W. Ni, T. Wang, P. A. Schouwink, Y. C. Chuang, H. M. Chen, X. Hu, *Angew. Chem. Int. Ed.* **2020**, *59*, 10797–10801; *Angew. Chem.* **2020**, *132*, 10889–10893.
[24] D. E. Brown, M. N. Mahmood, M. C. M. Man, A. K. Turner, *Electrochim. Acta* **1984**, *29*, 1551–1556.
[25] J. R. McKone, B. F. Sadtler, C. A. Werlang, N. S. Lewis, H. B. Gray, *ACS Catal.* **2013**, *3*, 166–169.
[26] Y. Duan, Z.-Y. Yu, L. Yang, L.-R. Zheng, C.-T. Zhang, X.-T. Yang, F.-Y. Gao, X.-L. Zhang, X. Yu, R. Liu, H.-H. Ding, C. Gu, X.-S. Zheng, L. Shi, J. Jiang, J.-F. Zhu, M.-R. Gao, S.-H. Yu, *Nat. Commun.* **2020**, *11*, 4789.
[27] M. Rajamathi, P. V. Kamath, R. Seshadri, *Mater. Res. Bull.* **2000**, *35*, 271–278.
[28] D. S. Hall, D. J. Lockwood, C. Bock, B. R. MacDougall, *Proc. Math. Phys. Eng. Sci.* **2015**, *471*, 20140792.
[29] D. Carriazo, C. Domingo, C. Martin, V. Rives, *Inorg. Chem.* **2006**, *45*, 1243–1251.
[30] N. Han, F. Zhao, Y. Li, *J. Mater. Chem. A* **2015**, *3*, 16348–16353.
[31] Y. Y. Chen, Y. Zhang, X. Zhang, T. Tang, H. Luo, S. Niu, Z. H. Dai, L. J. Wan, J. S. Hu, *Adv. Mater.* **2017**, *29*, 1703311.
[32] Y. An, X. Long, M. Ma, J. Hu, H. Lin, D. Zhou, Z. Xing, B. Huang, S. Yang, *Adv. Energy Mater.* **2019**, *9*, 1901454.
[33] Y. Song, E. Ozdemir, S. Ramesh, A. Adishev, S. Subramanian, A. Harale, M. Albuali, B. A. Fadhel, A. Jamal, D. Moon, S. H. Choi, C. T. Yavuz, *Science* **2020**, *367*, 777–781.
[34] Y. Wang, G. Wang, G. Li, B. Huang, J. Pan, Q. Liu, J. Han, L. Xiao, J. Lu, L. Zhuang, *Energy Environ. Sci.* **2015**, *8*, 177–181.
[35] A. G. Oshchepkov, A. Bonnefont, S. N. Pronkin, O. V. Cherstiouk, C. Ulhaq-Bouillet, V. Papaefthimiou, V. N. Parmon, E. R. Savinova, *J. Power Sources* **2018**, *402*, 447–452.
[36] G. L. Soloveichik, *Proc. IEEE* **2014**, *102*, 964–975.
[37] M. Zhou, Q. Weng, Z. I. Popov, Y. Yang, L. Y. Antipina, P. B. Sorokin, X. Wang, Y. Bando, D. Golberg, *ACS Nano* **2018**, *12*, 4148–4155.
[38] L. J. Yang, L. L. Zeng, H. Liu, Y. Q. Deng, Z. Q. Zhou, J. Y. Yu, H. Liu, W. J. Zhou, *Appl. Catal. B* **2019**, *249*, 98–105.
[39] P. Kuang, T. Tong, K. Fan, J. Yu, *ACS Catal.* **2017**, *7*, 6179–6187.
[40] P. Xiao, M. A. Sk, L. Thia, X. Ge, R. J. Lim, J.-Y. Wang, K. H. Lim, X. Wang, *Energy Environ. Sci.* **2014**, *7*, 2624–2629.
[41] S. P. Wang, J. Wang, M. L. Zhu, X. B. Bao, B. Y. Xiao, D. F. Su, H. R. Li, Y. Wang, *J. Am. Chem. Soc.* **2015**, *137*, 15753–15759.
[42] W. Chen, J. Pei, C. T. He, J. Wan, H. Ren, Y. Zhu, Y. Wang, J. Dong, S. Tian, W. C. Cheong, S. Lu, L. Zheng, X. Zheng, W. Yan, Z. Zhuang, C. Chen, Q. Peng, D. Wang, Y. Li, *Angew. Chem. Int. Ed.* **2017**, *56*, 16086–16090; *Angew. Chem.* **2017**, *129*, 16302–16306.
[43] J. K. Nørskov, T. Bligaard, A. Logadottir, J. R. Kitchin, J. G. Chen, S. Pandelov, U. Stimming, *J. Electrochem. Soc.* **2005**, *152*, J23–J26.
[44] L. Liu, Y. Liu, C. Liu, *J. Am. Chem. Soc.* **2020**, *142*, 4985–4989.

[45] D. Strmcnik, M. Uchimura, C. Wang, R. Subbaraman, N. Danilovic, D. van der Vliet, A. P. Paulikas, V. R. Stamenkovic, N. M. Markovic, *Nat. Chem.* **2013**, *5*, 300–306.

[46] T. Cheng, L. Wang, B. V. Merinov, W. A. Goddard, III, *J. Am. Chem. Soc.* **2018**, *140*, 7787–7790.

[47] J. Li, S. Ghoshal, M. K. Bates, T. E. Miller, V. Davies, E. Stavitski, K. Attenkofer, S. Mukerjee, Z. F. Ma, Q. Jia, *Angew. Chem. Int. Ed.* **2017**, *56*, 15594–15598; *Angew. Chem.* **2017**, *129*, 15800–15804.

[48] F. Song, W. Li, J. Yang, G. Han, P. Liao, Y. Sun, *Nat. Commun.* **2018**, *9*, 4531.

[49] J. A. Bau, S. M. Kozlov, L. M. Azofra, S. Ould-Chikh, A.-H. Emwas, H. Idriss, L. Cavallo, K. Takanabe, *ACS Catal.* **2020**, *10*, 12858–12866.